Real-time digital twin implementation of power electronics-based hydrogen production system

Deshmukh, Rohan Shailesh; Rituraj, Gautam; Bauer, Pavol; Vahedi, Hani

DOI
10.1016/j.egyr.2025.04.017

Publication date
2025

Document Version
Final published version

Published in
Energy Reports

Citation (APA)
Deshmukh, R. S., Rituraj, G., Bauer, P., & Vahedi, H. (2025). Real-time digital twin implementation of power electronics-based hydrogen production system. *Energy Reports*, *13*, 5006-5015. https://doi.org/10.1016/j.egyr.2025.04.017

Energy Reports 13 (2025) 5006–5015

Contents lists available at ScienceDirect

Energy Reports

journal homepage: www.elsevier.com/locate/egyr

Research paper

Real-time digital twin implementation of power electronics-based hydrogen production system

Rohan Shailesh Deshmukh *, Gautam Rituraj, Pavol Bauer, Hani Vahedi

Delft University of Technology, Mekelweg 4, Delft, 2628 CD, The Netherlands

ARTICLE INFO

Keywords:
Dual active bridge converter
Electrolyzer
Green hydrogen production
Real-time digital twin

ABSTRACT

This article implements a real-time digital twin (RTDT) of a 10 kW Dual Active Bridge (DAB)-electrolyzer system. The electrical model of a 10 kW alkaline electrolyzer is presented to understand its I–V characteristics. A sensitivity analysis is performed to assess the impact of various parameters on the electrolyzer's electrical characteristics. The series inductance, crucial for power transfer within a DAB converter, is examined using PLECS software to study the impact of the electrolyzer load on the peak and RMS currents. Based on this, the value of series inductance is optimized, resulting in a minimum overall RMS current throughout the operating power range. RTDT of the DAB electrolyzer system is developed using an OP4610XG real-time simulator to validate the presented model and simulation parameters. A comparison with the PLECS simulation results shows that the developed RTDT accurately operates within the 10 kW alkaline electrolyzer's electrical characteristics. Thus, this setup exhibits the potential to evaluate power electronics converter designs without a physical electrolyzer system.

Nomenclature

Abbreviations

AC	Alternating-Current
DAB	Dual Active Bridge
DC	Direct-Current
DT	Digital Twin
EMI	Electromagnetic Interference
EV	Electric Vehicle
FPGA	Field Programmable Gate Array
HF	High Frequency
HV	High Voltage
HVDC	High Voltage Direct Current
LF	Low Frequency
LV	Low Voltage
LVAC	Low Voltage Alternating Current
LVDC	Low Voltage Direct Current
MVAC	Medium Voltage Alternating-Current
MVDC	Medium Voltage Direct Current
PEC	Power Electronics Converter
PI	Proportional Integral
PV	Photovoltaic
PWM	Pulse Width Modulation
RES	Renewable Energy Sources
RMS	Root Mean Square
RTDT	Real-Time Digital Twin
SPS	Single Phase Shift Modulation
SST	Solid-State Transformer
STATCOM	Static VAR Compensator
w.r.t	with respect to

Constants

N_s	Number of series-connected cells
N_t	Turns ratio of transformer
s, t, v, w	Temperature dependent constants

* Corresponding author.
E-mail addresses: r.s.deshmukh@tudelft.nl (R.S. Deshmukh), g.rituraj@tudelft.nl (G. Rituraj), P.Bauer@tudelft.nl (P. Bauer), h.vahedi@tudelft.nl (H. Vahedi).

https://doi.org/10.1016/j.egyr.2025.04.017
Received 22 January 2025; Received in revised form 24 March 2025; Accepted 7 April 2025
Available online 25 April 2025

Variables

ϕ	Phase shift angle, rad
A_{elect}	Electrode surface area, m^2
a_{we}	Water activity of KOH solution
C_o	Output capacitance, F
d	Phase shift ratio
F	Faraday constant, C mol^{-1}
f_{sw}	Converter switching frequency, Hz
$i_{act(ano)}$	Anode activation current, A
$i_{act(cat)}$	Cathode activation current, A
$i_{L(rms)}$	RMS inductor current, A
i_L	Inductor current, A
I_{stack}	Average stack current, A
i_{stack}	Stack current, A
I_n	Inductor state currents, A
k	Voltage gain
L	Inductor/Inductance, H
P_{abs}	Absolute pressure, bar
P_o	Rated power, W
$P_{v(KOH)}$	Vapor pressure of KOH, bar
R	Universal gas constant, $JK^{-1}mol^{-1}$
r	Area-specific resistance of one of the electrolytic cells, Ωm^2
R_d	Lumped resistance, Ω
R_{int}	Internal resistance of the electrolyzer cell, Ω
R_{stack}	Stack resistance, Ω
T_c	Cell temperature, K
T_s	Switching period, s
t_n	Time instants, s
V^0_{rev,T_c}	Temperature dependent reversible voltage, V
$v_{act(ano)}$	Anode activation potential, V
$v_{act(cat)}$	Cathode activation potential, V
V_{DC}	Input DC link voltage, V
V_{int}	Ohmic potential, V
V_o	Converter output voltage, V
V_{rev}	Reversible cell voltage, V
V_{stack}	Average stack voltage, V
z	Number of moles of electrons transferred for one mol of product

1. Introduction

Green hydrogen is poised to become an essential component of net-zero emissions. It serves various pivotal roles. These include acting as a zero-emission transportation fuel and carbon-neutral raw material for industry (Bonab and Yazdani-Asrami, 2025, 2024). Additionally, it functions as a conduit for renewable energy. Lastly, it is a storage solution to stabilize fluctuating power grids. Consequently, the technology for producing hydrogen without emissions is also gaining prominence and becoming central to the energy transition (Linde, 2024). Currently, electrolysis stands as the predominant method for green hydrogen production (Bonab et al., 2024). This process involves separating water into hydrogen and oxygen through electricity from renewable energy sources. The equipment used for this purpose is referred to as electrolyzers. Currently, only 0.1% of global hydrogen production is derived from renewable energy sources powered by water electrolyzers and is classified as green (Green Hydrogen Coalition, 2022). According to the Global Hydrogen Review, 2022, global electrolyzer capacity could reach 134 GW by 2030 based on the current project pipeline (International Energy Agency, 2022).

Power electronics interfaces are vital in integrating such RESs with electrolyzers. Typically, electrolyzers are interfaced with conventional AC distribution systems with either a single conversion stage (AC/DC) or an additional (optional) DC/DC conversion stage. Fig. 1(a) showcases the conventional electrolyzer plant based on the MVAC system (Koponen et al., 2018; Chen et al., 2022). This system consists of RES, such as wind turbines and PV farms connected to the AC distribution system using AC/AC and DC/AC converters, respectively. The LF transformers step down the voltage for MVAC and LVAC distribution systems. Finally, the AC/DC converters interface the electrolyzer via an LVDC distribution system. It is important to note that the AC/DC conversion stage (rectifier) is thyristor-based.

Thyristor-based AC/DC power converters have long been the preferred solution for high-power AC/DC applications due to their robustness, high efficiency, and low cost (Siebert et al., 2002; Solanki et al., 2015a; Rodríguez et al., 2005; Solanki et al., 2015b). Nevertheless, it also introduces power quality issues related to current harmonics and low power factor on the AC side when operated at a larger firing angle past the nominal operation point. As a result, harmonic filters/compensators such as active power filters or STATCOMs and/or passive filters are required to control the power quality of the distribution grid. Furthermore, the requirement of bulky LF transformers increases the overall system costs (Solanki et al., 2015a). Thyristor rectifiers introduce a significant amount of current ripple on the DC side (Hernández-Gómez et al., 2021; Dobó and Palotás, 2017). Since the stack current of the electrolyzer controls the average hydrogen production rate (Koponen et al., 2018), thyristor switch-based rectifiers have a detrimental impact on the electrolyzer operation.

Fig. 1(b) showcases a relatively similar electrolyzer system based on a DC distribution system. DC/DC converters have been utilized to interface several RESs with the grid and the HVDC grid with the MVDC grid. Finally, electrolyzers are interfaced with the MVDC grid using DC/DC converters. Contrary to the system shown in Fig. 1(a), each DC/DC converter can be operated at a higher switching frequency, pushing the current harmonics to higher orders and minimizing them. The size of the high-frequency transformer and the filter capacitor in the case of isolated DC/DC converters can be significantly reduced. As a result, the DC-based electrolyzer power plant may exhibit significant potential compared to its AC counterpart. This paper considers the DC-based electrolyzer power plant. Designing such power electronics interfaces is not straightforward for electrolyzer systems scaled up to an industrial level. DC–DC converters designed for electrolyzers must meet several requirements, which include (Guilbert et al., 2017; El Kattel et al., 2024):

1. High efficiency over a wide operating range (large DC voltage gain),
2. High power density,
3. EMI,
4. Smaller output current ripple,
5. Low cost, and
6. Reliability in the case of power switch failures.

In addition to the listed requirements, the converter under design must incorporate galvanic isolation conforming with ISO:22734:2020 and ISO:19880-1:2020 standards. Given the nature of electrolysis, it should be capable of operating at low voltage and extremely high current.

Based on the literature review conducted in Deshmukh et al. (2022), isolated DC–DC converter topologies are prime candidates for such an integration. Among the various isolated DC–DC converter topologies, the DAB Converter exhibits much potential as a power electronics interface for electrolyzers. This topology has been utilized in a plethora of applications such as in DC grids (Zhao et al., 2012a; Wen et al.,

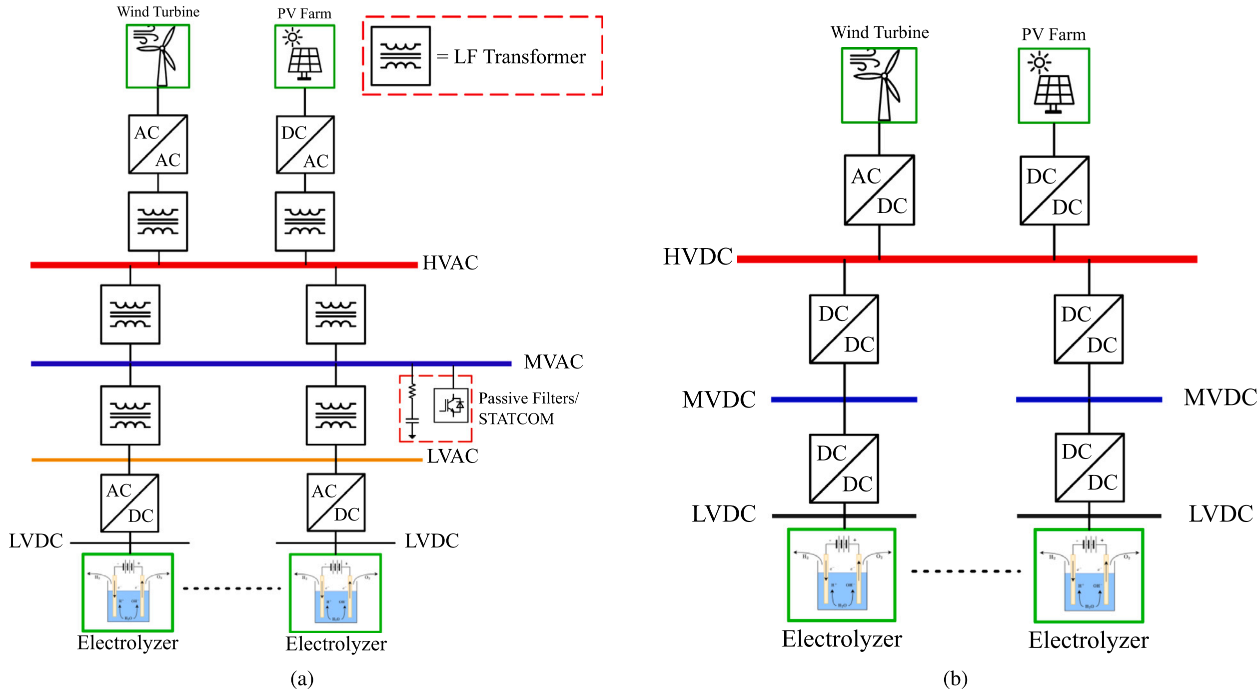

Fig. 1. Electrolyzer power plant (a) AC grid-based and (b) DC grid-based.

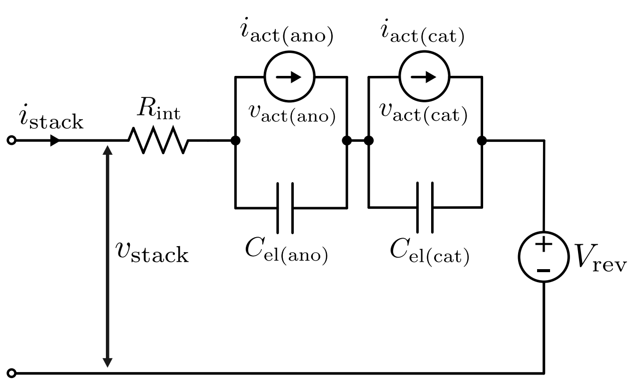

Fig. 2. Electrical model of an alkaline electrolyzer.

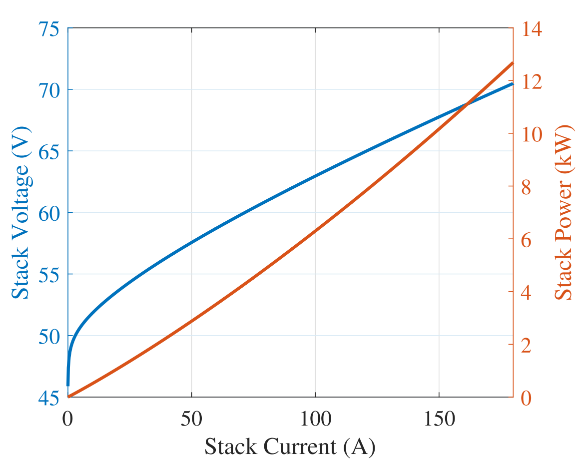

Fig. 3. Electrical characteristics of a 10 kW alkaline electrolyzer for stack temperature, T_c = 15 °C.

2014; Zhao et al., 2013), SSTs (Shi et al., 2011; Zhao et al., 2012b; She et al., 2013), etc. DAB converter offers several advantages. The inherent ability to achieve soft-switching, galvanic isolation between the high voltage and the low voltage side via HF transformer, and high efficiency (Oggier et al., 2010; Krismer and Kolar, 2011) over a wide operating region are the most important advantages from the context of electrolysis.

Testing and evaluating PECs for electrolysis remains challenging due to the safety concerns associated with hydrogen gas. Since most power supplies for electrolyzers are integrated within the chassis, any abnormal behavior or fault exhibited by the converter during the testing phase might trigger hazardous conditions. To evaluate the performance of a designed PEC for the electrolyzer, a DT can be developed. It is a virtual representation of a physical PEC, including its characteristics, behavior, and performance (Deshmukh et al., 2023a). As a result, PEC can be tested for a wide number of scenarios without the requirement of an actual electrolyzer. DTs have been widely utilized for various applications, such as aerospace (Glaessgen and Stargel, 2012), power systems (Zhou and Yan, 2018; Moutis and Alizadeh-Mousavi, 2020), EVs (Venkatesan et al., 2019), and HIL simulation to validate controllers and conduct scenario and risk assessments (Rasheed et al., 2020). However, few works have explored DT for electrolyzer (Shin et al., 2022; Zhang et al., 2022b).

This article builds upon the ideas of our preliminary work presented in Deshmukh et al. (2022, 2023a,b), offering additional contributions:

1. The activation potential was considered to be negligible in Deshmukh et al. (2022) to simplify the modeling process and for study purposes. However, this work includes the impact of activation potential, thereby transitioning to the detailed electrolyzer model.
2. Studies on electrolyzers have been carried out from the perspective of electrochemistry. For instance, literature for electrolyzers exists for topics such as type of electrode materials (Pham et al., 2021; Zhang et al., 2022a; Bodner et al., 2015), and time variation effects (LeRoy et al., 1979). However, the study on the impact of electrolyzer parameters on electrical characteristics is more relevant from the context of PEC design. This work

provides a sensitivity analysis of the detailed electrolyzer model to highlight how various electrolyzer parameters influence its electrical characteristics.
3. The series inductance within a DAB converter needs to be appropriately chosen, as it not only influences the peak and RMS currents of the converter but also impacts the shape of the current waveform. Studies based on the choice of the series inductance for a DAB converter specifically for electrolysis have not been found in the literature. Therefore, expressions for the output power, series inductance, and piece-wise function for the peak current of the DAB converter during electrolysis were derived to examine the effects of series inductance on the DAB converter's peak and RMS currents, considering the electrolyzer's operating power variation. Based on these expressions, an optimal value of inductance is chosen to achieve minimum RMS current throughout the operating power region of the electrolyzer. Compared to Deshmukh et al. (2023b), the extended work utilizes a PI-based current control approach to track the stack current compared to the PI-based power control approach.
4. A RTDT of a DAB converter integrated with a 10 kW alkaline electrolyzer has been implemented in an OPAL-RT real-time simulator, extending beyond the open-loop implementation in Deshmukh et al. (2023a). The operation of the RTDT is validated with the PLECS simulation.

The structure of the paper is as follows: Section 2 provides a detailed electrical model of a 10 kW alkaline electrolyzer. A sensitivity analysis is conducted to study the impact of various electrolyzer parameters on the electrical characteristics. Section 3 presents the DAB converter. It includes a multi-parameter sweep analysis for selecting the series inductance for the DAB converter. Section 4 describes the implementation of the RTDT, and presents the results and the validation of the RTDT model based on the selected series inductance. Finally, Section 5 provides the conclusions.

2. Electrolyzer modeling and sensitivity analysis

From a PEC design perspective, the relevant electrical parameters of an electrolyzer are the stack voltage and current. In the literature, several modeling approaches (Ulleberg, 2003; Falcão and Pinto, 2020; Ursúa and Sanchis, 2012; Gallandat et al., 2017) have been proposed. The method proposed in Ursúa and Sanchis (2012) is adopted in this work. As shown in Fig. 2, the stack voltage of an electrolyzer constitutes four potentials: reversible stack potential, activation potential, ohmic potential, and diffusion potential. For this modeling, the diffusion potential has been considered negligible and, therefore, has not been considered. Eq. (1) defines the reversible stack potential (Ursúa and Sanchis, 2012). It exhibits the thermodynamic phenomena in the electrolysis reaction.

$$V_{\text{rev}} = N_{\text{s}}\left(V^{0}_{\text{rev},\text{T}_{\text{c}}} + \frac{RT_{\text{c}}}{zF}\log\left(\frac{(P_{\text{abs}} - P_{\text{v(elec)}})^{1.5}}{a_{\text{we}}}\right)\right) \tag{1}$$

Eqs. (2) and (3) define the electrode activation potentials for anode and cathode, respectively (Ursúa and Sanchis, 2012). These activation potentials are related to the anode and cathode capacitances, $C_{\text{el(ano)}}$, and $C_{\text{el(cat)}}$, respectively. This potential also refers to the double layer effect formed at the cell's cathode (Aikens, 1983).

$$v_{\text{act(ano)}} = sN_{\text{s}}\ln\left(\frac{i_{\text{act(ano)}}}{t} + 1\right) \tag{2}$$

$$v_{\text{act(cat)}} = vN_{\text{s}}\ln\left(\frac{i_{\text{act(cat)}}}{w} + 1\right) \tag{3}$$

Finally, Eq. (4) refers to the ohmic potential, which can be defined as the voltage drop across the internal resistance (electrolyte) between the two electrodes (Ursúa and Sanchis, 2012).

$$V_{\text{int}} = N_{\text{s}}i_{\text{stack}}R_{\text{int}} = N_{\text{s}}i_{\text{stack}}\frac{r}{A_{\text{elect}}} \tag{4}$$

Note, that the temperature-dependent constants and area-specific resistance values have been directly collected from Ursúa and Sanchis (2012) for the modeling process in this work.

The total stack voltage of an alkaline electrolyzer can be obtained as the sum of the potentials mentioned in (1)–(4).

$$v_{\text{stack}} = V_{\text{rev}} + v_{\text{act(ano)}} + v_{\text{act(cat)}} + V_{\text{int}} \tag{5}$$

Fig. 3 showcases the I–V and I–P characteristics of a 10 kW alkaline electrolyzer operating at a stack temperature of 15 °C. The characteristics indicate a wide operating range of the electrolyzer. In addition to the stack temperature, other parameters govern the operation of an electrolyzer that, in turn, may also impact its electrical behavior. These parameters include stack pressure, molar concentration of the electrolyte, electrode cross-sectional area, and activation current. It has been proved experimentally in Ursúa and Sanchis (2012) that stack pressure does not impact the electrolyzer's electrical characteristics; therefore, this parameter will not be considered in this work. It is essential to conduct a sensitivity analysis on the electrolyzer model to study the effect of these parameters on the electrical characteristics.

Figs. 4(a)–4(d) show the impact on the electrical characteristics for variation in stack temperature, molar concentration, electrode cross-sectional area, and activation current, respectively. The stack temperature shifts the characteristics along the stack voltage axis, as shown in Fig. 4(a). A higher stack temperature accelerates the rate of chemical reaction, thereby improving the hydrogen yield but at the cost of a lower stack voltage. Little or no variation is observed from the electrical perspective in case of variation in the molar concentration of the electrolyte, as illustrated in Fig. 4(b). However, a higher molar concentration leads to a more corrosive electrolyte, which can degrade the electrodes and inner body of the electrolyzer. The choice of electrode cross-sectional area directly affects the internal resistance per (4). While a smaller electrode surface area increases the stack voltage for a given stack current, as depicted in Fig. 4(c), it leads to considerable internal resistance (higher ohmic potential), decreasing the electrolyzer's efficiency. On the other hand, a large cross-sectional area of the electrode leads to a decrease in stack voltage for a given stack current; however, this improves the electrolyzer's efficiency at the cost of opting for semiconductor switches with higher current ratings and thermal handling capability. The size of the electrolyzer also limits the cross-sectional area of the electrode. Activation current is required to overcome the double-barrier effect formed due to electric charge transfer between the chemical species and the electrodes. Fig. 4(d) shows curves for various percentage loading of activation current. A lower activation current leads to a lower stack voltage as it is more difficult to overcome the double-barrier effect.

3. DAB converter

Fig. 5 illustrates the DAB converter, composed of two H-bridges: the H-HV and H-LV. These denote the high-voltage side bridge (referred to as the leading H-bridge) and the low-voltage side bridge (referred to as the lagging H-bridge). Each bridge is separated by an HF transformer for isolation in various applications. This study employs the SPS strategy as the conventional control approach within the industry. Fig. 6 illustrates the SPS strategy. Eqs. (6)–(8) govern the operation of the DAB converter under the SPS strategy.

$$P_{\text{o}} = \frac{V_{\text{DC}}V_{\text{o}}N_{\text{t}}(d(1-d))}{2f_{\text{sw}}L} \tag{6}$$

$$N_{\text{t}} = \frac{V_{\text{DC}}}{V_{\text{o}}} \tag{7}$$

$$d = \frac{\phi}{\pi} \tag{8}$$

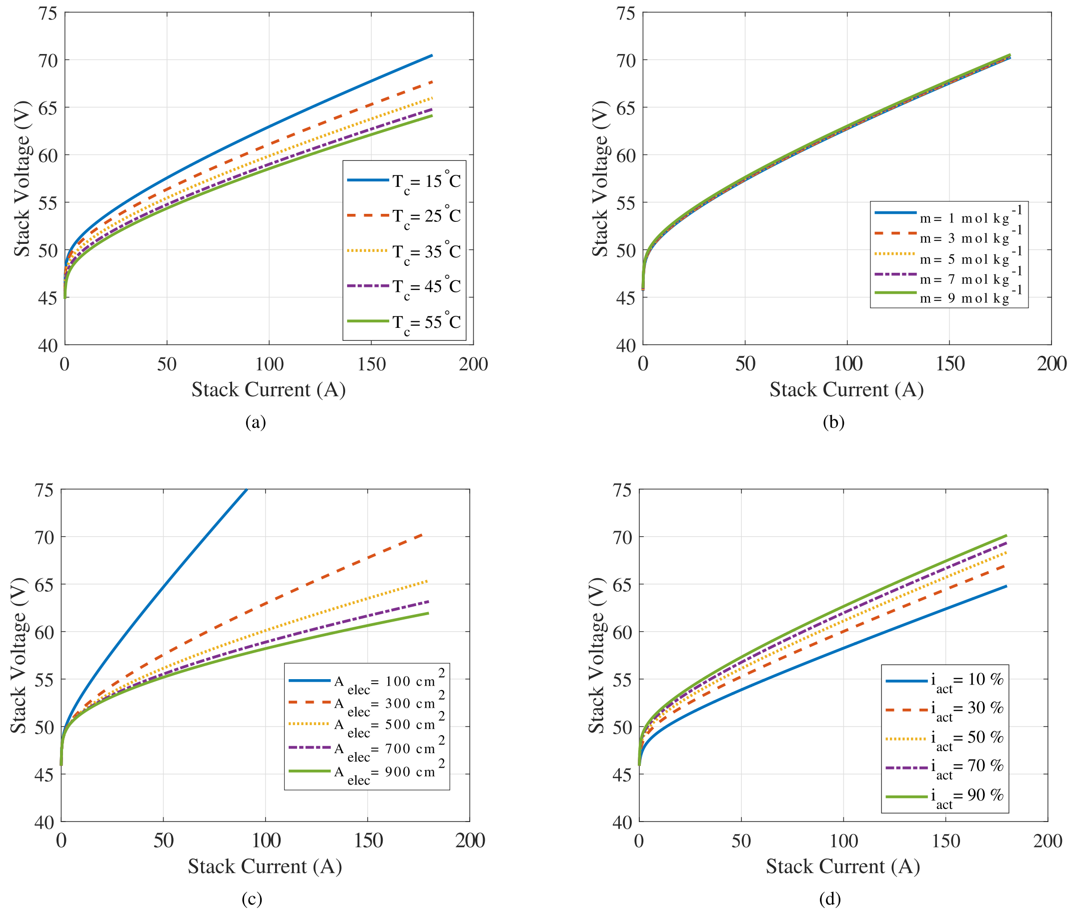

Fig. 4. Sensitivity analysis conducted on a 10 kW electrical model of an alkaline electrolyzer showing the effect of (a) Stack temperature, (b) Molar concentration of electrolyte, (c) Electrode surface area, and (d) Activation current on the electrical characteristics of the electrolyzer (legend refers to the percentage of the rated activation current).

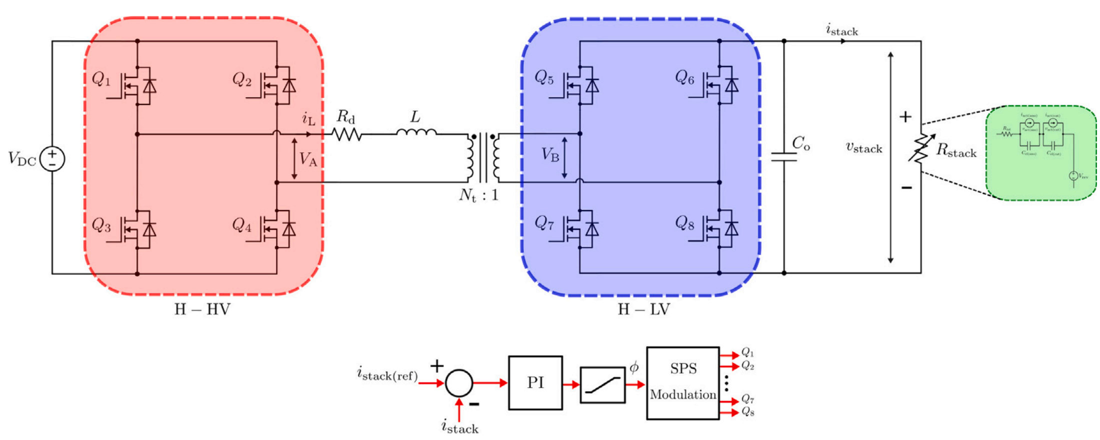

Fig. 5. Dual active bridge converter integrated with the electrical model of an alkaline electrolyzer.

3.1. Effect of series inductance

The DAB converter depicted in Fig. 5 can be represented by a simplified equivalent circuit, as shown in Fig. 7. This reduced circuit configuration comprises two voltage sources, V_A and $N_t V_B$ (referred to as the primary side) linked by L, which facilitates power transfer between the high and low-voltage sides. L permits power flow and influences the waveform of the inductor current. In fixed voltage or linear load applications, choosing L is relatively straightforward, guided by the converter's designated operating power. However, during electrolysis, the output voltage and current are dynamic, exhibit non-linear behavior, and change over time. Under these conditions, the choice of L is critical to ensure that the transformer current waveform maintains minimal peak and RMS values across the extensive operational range defined by the electrolyzer's electrical properties. This choice impacts the current ratings of semiconductor switches.

3.2. Effect of electrolysis on series inductance, RMS and peak currents

A parameter sweep-based simulation was conducted in PLECS to quantitatively understand the impact of the choice of series induc-

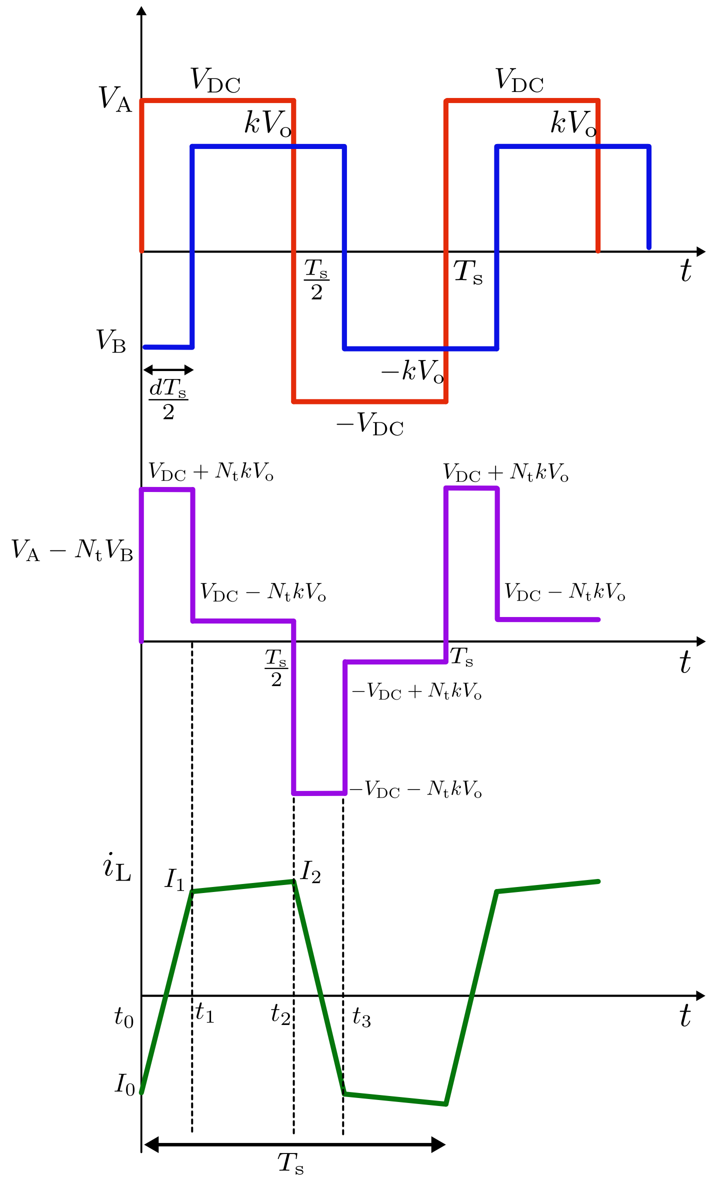

Fig. 6. SPS Modulation in DAB converter.

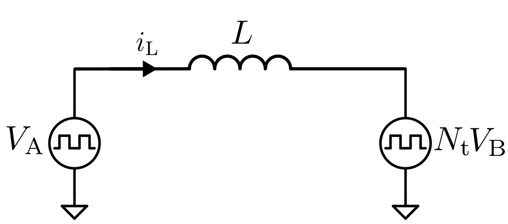

Fig. 7. Simplified equivalent circuit of the DAB converter.

tance and explore the effect of electrolysis on the selection of series inductance. For this study, the transformer is assumed to be ideal, and therefore, the magnetizing inductance is sufficiently large to prevent saturation. A simple closed loop current control is built to automate the sweep process, which regulates the phase angle, ϕ, as shown in Fig. 5. Additionally, the alkaline electrolyzer has been implemented in the form of a non-linear variable resistor given by,

$$R_{stack} = \frac{v_{stack}}{i_{stack}} \tag{9}$$

The value of R_{stack} is varied using a lookup table based on the I–V characteristics described in Fig. 3 corresponding to the 15 °C curve. Substituting (5) in (6), we have the output power of the DAB converter during electrolysis,

$$P_o = \frac{V_{DC}N_tN_sRd(1-d)}{2Lf_{sw}zF}\left(T_c\log\left(\frac{(P_{abs}-P_{v,KOH})^{1.5}}{a_{we}}\right)\right.$$
$$\left.+\frac{zF}{R}\left(V_{rev}^0+s\log\left(\frac{i_{act,a}}{t}+1\right)+v\log\left(\frac{i_{act,c}}{w}+1\right)+V_{int}\right)\right) \tag{10}$$

Rearranging (10), the inductance of the DAB converter for electrolysis during SPS modulation can be expressed as,

$$L = \frac{V_{DC}N_tN_sRd(1-d)}{2P_of_{sw}zF}\left(T_c\log\left(\frac{(P_{abs}-P_{v,KOH})^{1.5}}{a_{we}}\right)\right.$$
$$\left.+\frac{zF}{R}\left(V_{rev}^0+s\log\left(\frac{i_{act,a}}{t}+1\right)+v\log\left(\frac{i_{act,c}}{w}+1\right)+V_{int}\right)\right) \tag{11}$$

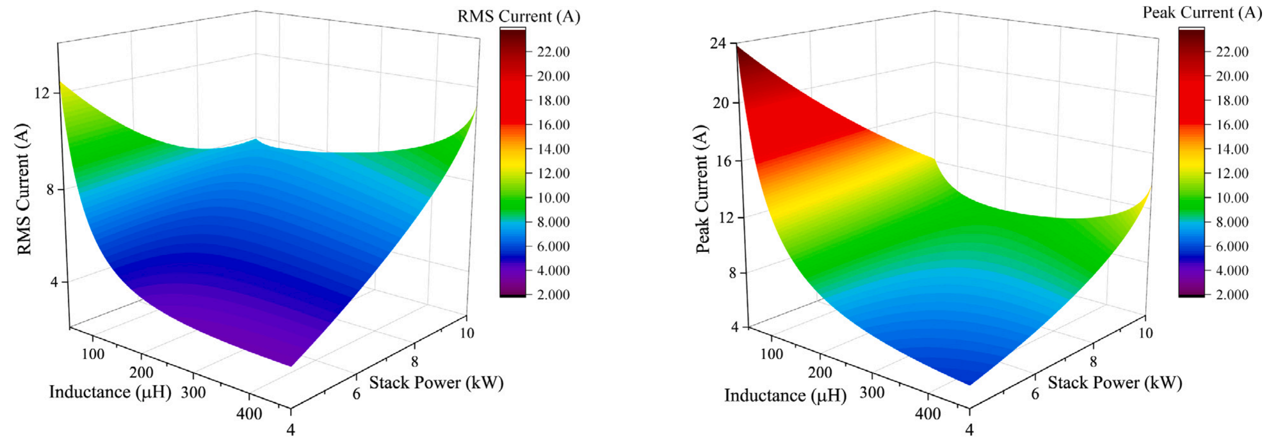

(a) (b)

Fig. 8. Effect of electrolysis on DAB converter's primary (a) RMS current and (b) Peak current, with varying operating power and series inductance.

Table 1
Real-time simulator specifications.

(a) Target Computer Specifications	
	Description
Model	OP4610XG
Operating System	OPAL-RT Linux 3.4.1
Central Processing Unit (CPU)	AMD Ryzen 5 3600XT, 6-Core, 3.8 GHz
Memory (RAM)	8 GB
Motherboard	X570D4U-2L2T AsRock uATX Server Motherboard, AMD socket AM4 PGA 1331 Dual 10GLAN
AC Input	100–240 V, 50–60 Hz
(b) FPGA Specifications	
	Description
Model	Kintex 7 TE0741
Operating System	OPAL-RT Linux 3.4.1
Number of Analog Channels	16 (Both input and output)
Analog Input Card Model	OP5340 (Input Range: ±20 V to ±30 V)
Analog Output Card Model	OP5330 (Output Range: ±5 V, ±10 V, ±16 V)
Number of Digital Channels	32 (Bidirectional)
Digital input–output card model	OP5369
Digital input specifications:	Voltage Range: 0 to 30 V DC, Turn-on delay: 10 ns, Turn-off delay: 15 ns
Digital output specifications	Voltage range: 4.5 to 25 V DC, Turn on delay: <90 ns (5 V) and <100 ns (25 V) Turn off delay: <90 ns (5 V) and <100 ns (25 V)
Output Frequency	up to 4 MHz

Eqs. (10)–(11) relate the DAB converter parameters with the electrolyzer parameters. This relationship showcases that component selection for a DAB converter is no longer dependent only on the output power of the converter but also on electrolyzer parameters such as the activation current, vapor pressure, water activity, stack temperature, etc.

The converter's operating power and the series inductance were adjusted while connected to the alkaline electrolyzer electrical model. Given that the electrolyzer's operating power can range from 40% to 100% of its rated capacity, the peak and RMS currents were calculated for each combination of operating power and series inductance.

Fig. 8 illustrates the variations in primary peak and RMS currents resulting from changes in the converter's series inductance and operating power for a 10 kW alkaline electrolyzer. As shown in Fig. 8(a), the RMS currents exhibit an inverse relationship with the operating power for lower values of series inductance. On the other hand, as the value of series inductance increases, the RMS currents increase with operating power; therefore, this relationship transitions towards a direct one. For lower values of operating power (4 kW $\leq P_o \leq$ 6 kW), the RMS currents hold an inverse relationship with the series inductance. However, as the electrolyzer tends to operate towards the rated power of P_o = 10 kW, the RMS currents exhibit little or no significant variation over the range of series inductance. A similar trend is observed in the peak current over the operating power range, as shown in Fig. 8(b). The series inductance was selected to ensure a minimum RMS current value over the operating power range.

From Fig. 6, it is evident that the inductor current, i_L can be expressed as a piece-wise function,

$$i_L(t) = \begin{cases} I_0 + \left(\frac{I_1 - I_0}{t_1}\right) t, & t_0 \leq t < t_1, \\ I_1 + \left(\frac{I_2 - I_1}{t_2 - t_1}\right)(t - t_1), & t_1 \leq t < t_2, \\ I_2 - \left(\frac{-I_0 + I_2}{t_3 - t_2}\right)(t - t_2), & t_2 \leq t < t_3, \\ I_0 - \left(\frac{I_0 + I_1}{T_s - t_3}\right)(t - t_3), & t_3 \leq t < T_s \end{cases} \tag{12}$$

where

$$t_0 = 0, \quad t_1 = \frac{dT_s}{2}, \quad t_2 = \frac{T_s}{2}, \quad t_3 = \frac{(1+d)T_s}{2},$$

$$I_0 = -\frac{V_{DC}(k(2d-1)+1)}{4Lf_{sw}}, \quad I_1 = \frac{V_{DC}(2d+k-1)}{4Lf_{sw}}, \quad I_2 = \frac{V_{DC}(k(2d-1)+1)}{4Lf_{sw}}, \text{ and}$$

$$k = \frac{v_{stack}}{V_o}.$$

The RMS current, $i_{L(rms)}$ can therefore, be calculated as

$$i_{L(rms)} = \sqrt{\sum_{n=1}^{N} \frac{1}{t_n - t_{n-1}} \int_{t_{n-1}}^{t_n} [i_L(t)]^2 \, dt} \tag{13}$$

The selection of inductance for the considered electrolyzer was determined based on the following optimization problem,

$$\begin{aligned} \underset{i_{L(rms)}}{\text{minimize}} \quad & i_{L(rms)}(L, P_o) \\ \text{subject to} \quad & 50\ \mu\text{H} \leq L \leq 450\ \mu\text{H} \\ & 4\ \text{kW} \leq P_o \leq 10\ \text{kW} \end{aligned} \tag{14}$$

Solving (14), for the specified operating power range, and for the series inductance range, it was found that a series inductance selected in the range, 230 μH $\leq L \leq$ 240 μH provided an average RMS current of approximately 5.96 A, which corresponds to the lowest average RMS value over the operating power range. As a result, a value of L = 235 μH was selected for this work.

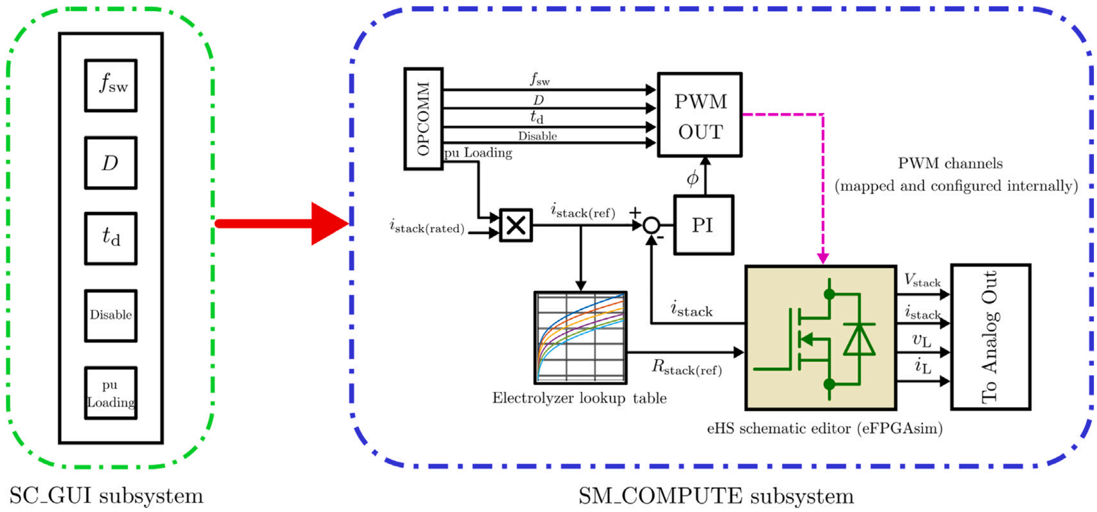

Fig. 9. Detailed structure of the closed-loop RTDT of a DAB converter integrated with the 10 kW alkaline electrolyzer.

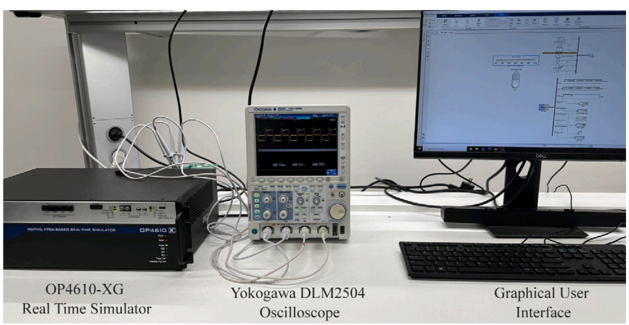

Fig. 10. RTDT setup.

Table 3
Comparison of RTDT model with PLECS model for 15 °C stack temperature.

Operating power case	Method	V_{stack} (V)	I_{stack} (A)	$i_{L(rms)}$ (A)	i_{peak} (A)	P_{stack}	% Error (P_{stack}) w.r.t PLECS
10 kW	RTDT	67.38	147.5	7.52	9	9.93	0.7%
	PLECS	67.55	148.46	8.1	9.2	10	
8 kW	RTDT	64.94	122.38	6.04	8.2	7.95	0.63%
	PLECS	65.17	122.71	6.54	8.37	8	
6 kW	RTDT	62.5	96	4.72	7.4	6	0%
	PLECS	62.53	95.92	5.16	7.73	6	
4 kW	RTDT	59.5	67.63	3.78	7	4.02	−0.5%
	PLECS	59.51	67.2	4.14	7.33	4	

Table 2
Test converter specifications.

Parameter	Value	Parameter	Value
P_o	10 kW	R_d	0.1 Ω
V_{DC}	1400 V	L	235 μH
V_o	70 V	f_{sw}	50 kHz
N_t	20:1	C_o	440 μF

4. Results and discussion

A MATLAB Simulink model is unsuitable for direct real-time simulation on OPAL-RT, requiring adaptation for such use. This has been illustrated in Fig. 9. The model is organized into two subsystems: SC_GUI for monitoring and input (e.g., switching frequency, duty cycle, dead time) and SM_COMPUTE for computations, including the plant model on the FPGA/CPU. The SC_GUI communicates with SM_COMPUTE via an OPCOMM block, simulating real-time links. While the CPU can compute with a minimum time step of 5 μs, higher switching frequencies, typical in power electronics, necessitate using the FPGA for faster computations. The eHS toolbox handles real-time power electronics simulations, integrating inputs and outputs between Simulink and the FPGA. For the current DAB converter system, PWM signals control the semiconductor switches, mapped to the FPGA via the eHS editor, with a 120 ns FPGA time step. A PI current controller adjusts the phase angle to regulate stack current, with the electrolyzer modeled as a variable resistor.

A test case was conducted to validate the RTDT. Fig. 10 depicts the RTDT setup. Table 1 provides the specifications of OP4610-XG real-time simulator used for this work. Table 2 presents the specifications of the DAB converter used for validation.

The alkaline electrolyzer within the RTDT was operated from 40% to 100% of the rated power, with the model's stack current loading ranging from 0.4 pu to 1 pu. Fig. 11 displays the RTDT model outputs, such as stack voltage, stack current, inductor voltage, and inductor current, as monitored on the Yokogawa DLM2504 oscilloscope connected to the analog output card of the simulator. The oscilloscope readings, which ranged up to ±16 V, corresponded to the output voltage range of the simulator's analog out cards.

The inductor voltage, v_L (shown in orange), appears as a spike rather than a square pulse, with the pulse width corresponding to the applied phase shift, ϕ. This effect can be attributed to the analog card's sampling rate limitations. However, the inductor currents are accurately visualized by the RTDT. As the alkaline electrolyzer is modeled as a variable resistor, the stack voltage and current on the oscilloscope show minimal to no ripple. Table 3 compares the measurements of the RTDT and the PLECS simulation model for the considered operating power cases. From Table 3, it was observed that the measured values of V_{stack}, I_{stack}, and P_{stack} are matching well with the simulation results with an error of less than 1%. However, a slight variation was seen in the i_{rms} than the i_{peak} obtained from RTDT and simulation. The limit in the analog card sampling rate can justify this. While the analog card sampling rate did not affect the peak values of the inductor voltage, it did impact the RMS value since it is calculated over the switching period. As a result, this impact was reflected within the transformer currents. Based on the measured RMS current values for RTDT, the average RMS current over the operating power range was found to be 5.52 A, which is close to the calculated value, as given in Section 3.2. The RTDT measurements of stack voltage and current, reported in Table

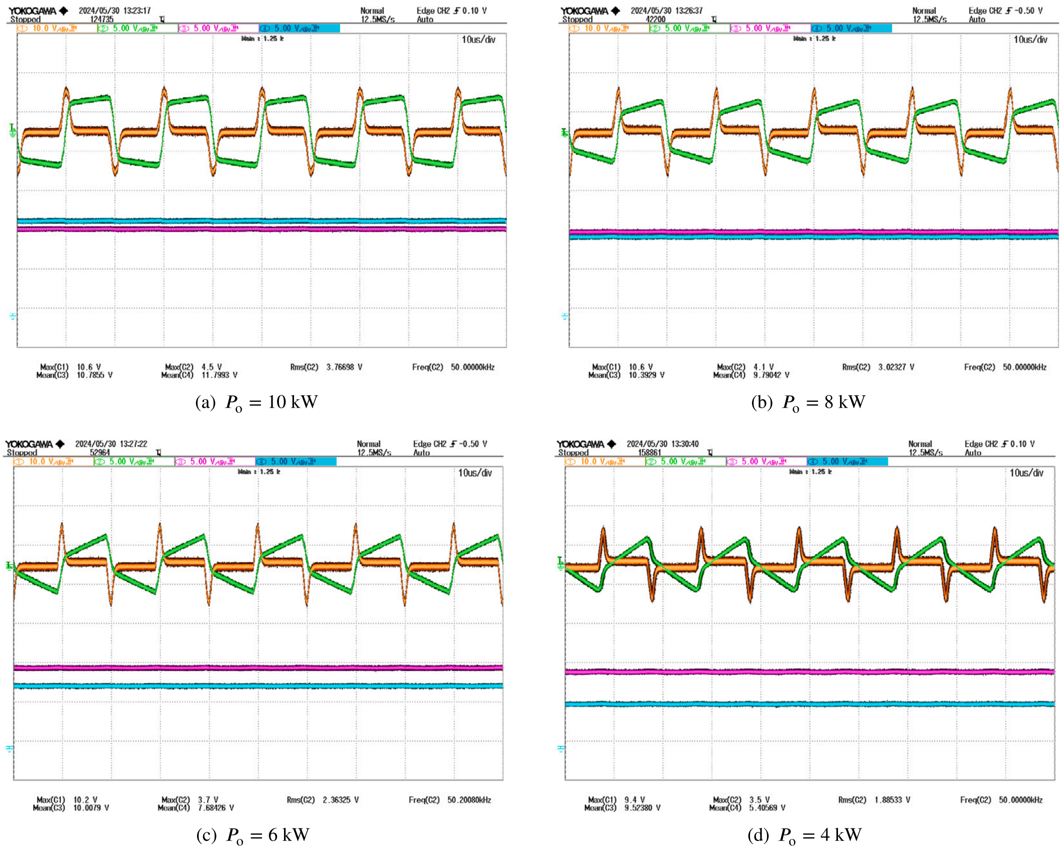

(a) $P_o = 10$ kW (b) $P_o = 8$ kW

(c) $P_o = 6$ kW (d) $P_o = 4$ kW

Fig. 11. Response of the closed loop RTDT of the DAB converter integrated with a 10 kW alkaline electrolyzer showcasing the inductor voltage (orange), the inductor current (green), stack voltage (purple), and stack current (cyan) at different operating powers.

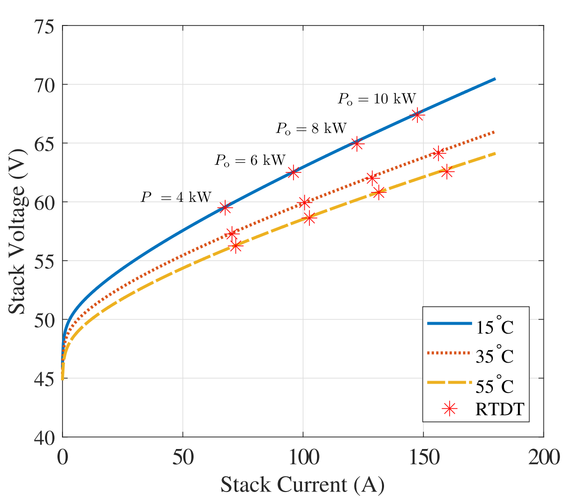

Fig. 12. Comparison of RTDT response with the electrolyzer I–V characteristics for variation in stack temperature.

3, were superimposed on the I–V characteristics of the electrolyzer operating at a temperature of $T_c = 15$ °C. To showcase the operation of RTDT during the variation in stack temperature, two additional characteristics were considered for $T_c = 35$ °C, and $T_c = 55$ °C, respectively. Fig. 12 showcases this superimposition and demonstrates that the PI current controller effectively tracks the reference stack current set-point, allowing the RTDT to operate along the electrical characteristics of the alkaline electrolyzer and during the variation in stack temperature.

5. Conclusions

This paper presents the implementation of an RTDT for a DAB converter with a 10 kW alkaline electrolyzer. A detailed electrical model of the electrolyzer was developed, incorporating activation potential, and a sensitivity analysis was conducted to assess the influence of various parameters on its electrical characteristics. Key findings of this work include:

- The selection of the DAB converter's series inductance, L, was studied due to its impact on transformer currents and the electrolyzer's variable operating conditions. Expressions for output power, series inductance, and a piecewise function for inductor current were derived.
- A multi-parameter sweep analysis using a PLECS-based closed-loop DAB model identified an optimal inductance of 235 μH, minimizing the average RMS current to 5.96 A over a 4–10 kW power range.
- A closed-loop RTDT of the DAB-electrolyzer system was developed, detailing its implementation, including the SC_GUI and SM_COMPUTE subsystems. The RTDT was validated at four power levels, considering stack temperature variations from 15 °C to 55 °C in steps of 20 °C.
- The RTDT model accurately replicated the electrolyzer's electrical characteristics and closely aligned with simulation results.

These results demonstrate the RTDT's potential for evaluating converter designs without requiring a physical electrolyzer and serve as a strong foundation for future assessments of power electronics converters in hydrogen production systems.

CRediT authorship contribution statement

Rohan Shailesh Deshmukh: Writing – review & editing, Writing – original draft, Visualization, Validation, Methodology, Investigation, Formal analysis, Conceptualization. **Gautam Rituraj:** Writing – review & editing, Visualization. **Pavol Bauer:** Supervision. **Hani Vahedi:** Supervision.

Declaration of competing interest

The authors declare that they have no known competing financial interests or personal relationships that could have appeared to influence the work reported in this paper.

Acknowledgments

This work was funded by Intelligent Power Electronics for High Power Quality of Electricity in Urban Areas with High Fraction of Renewables (IQGRID), Grant Number: TKI1621/1721.

Data availability

No data was used for the research described in the article.

References

Aikens, D., 1983. Electrochemical Methods, Fundamentals and Applications. ACS Publications.
Bodner, M., Hofer, A., Hacker, V., 2015. H2 generation from alkaline electrolyzer. Wiley Interdiscip. Rev.: Energy Environ. 4 (4), 365–381.
Bonab, S.A., Waite, T., Song, W., Flynn, D., Yazdani-Asrami, M., 2024. Machine learning-powered performance monitoring of proton exchange membrane water electrolyzers for enhancing green hydrogen production as a sustainable fuel for aviation industry. Energy Rep. 12, 2270–2282.
Bonab, S.A., Yazdani-Asrami, M., 2024. Investigation on the heat transfer estimation of subcooled liquid hydrogen for transportation applications using intelligent technique. Int. J. Hydrog. Energy 84, 468–479.
Bonab, S.A., Yazdani-Asrami, M., 2025. Artificial intelligence-based model to predict the heat transfer coefficient in flow boiling of liquid hydrogen as fuel and cryogenic coolant in future hydrogen-powered cryo-electric aviation. Fuel 381, 133323.
Chen, M., Chou, S.-F., Blaabjerg, F., Davari, P., 2022. Overview of power electronic converter topologies enabling large-scale hydrogen production via water electrolysis. Appl. Sci. 12 (4), 1906.
Deshmukh, R.S., Rituraj, G., Lock, N., Vahedi, H., Shekhar, A., Bauer, P., 2023a. Implementation of real-time digital twin of dual active bridge converter in electrolyzer applications. In: IECON 2023-49th Annu. Conf. IEEE Indus. Electron. Soc.. IEEE, pp. 1–6.
Deshmukh, R.S., Rituraj, G., Vahedi, H., Shekhar, A., Bauer, P., 2023b. Impact of electrolyzer on the operation of a dual active bridge converter. In: IECON 2023-49th Annu. Conf. IEEE Indus. Electron. Soc.. IEEE, pp. 1–6.
Deshmukh, R.S., Shekhar, A., Bauer, P., 2022. Adaptive modularity for power electronics based electrolysis systems for green hydrogen. In: 2022 IEEE 20th Int. Power Electron. Motion Control Conf.. PEMC, IEEE, pp. 508–515.
Dobó, Z., Palotás, Á.B., 2017. Impact of the current fluctuation on the efficiency of alkaline water electrolysis. Int. J. Hydrog. Energy 42 (9), 5649–5656.
El Kattel, M.B., Praça, P.P., Mayer, R., Lucio Berrehil el Kattel, C.d.C., Bascopé, R.P.T., Antunes, F.L.M., de Jesus Cardoso Filho, B., 2024. Overview of main electrolyzer technologies and power electronic converter topologies for enabling hydrogen production through water electrolysis. Int. J. Circuit Theory Appl.
Falcão, D., Pinto, A., 2020. A review on PEM electrolyzer modelling: Guidelines for beginners. J. Clean. Prod. 261, 121184.
Gallandat, N., Romanowicz, K., Züttel, A., 2017. An analytical model for the electrolyser performance derived from materials parameters. J. Power Energy Eng. 5 (10), 34–49.
Glaessgen, E., Stargel, D., 2012. The digital twin paradigm for future NASA and US air force vehicles. In: 53rd AIAA/ASME/ASCE/AHS/ASC Structures, Structural Dynamics and Materials Conf. 20th AIAA/ASME/AHS Adaptive Structures Conf. 14th AIAA. p. 1818.
Green Hydrogen Coalition, 2022. Green Hydrogen Guide Book. https://www.ghcoalition.org/guidebook. (Accessed: 21 October 2024).
Guilbert, D., Collura, S.M., Scipioni, A., 2017. DC/DC converter topologies for electrolyzers: State-of-the-art and remaining key issues. Int. J. Hydrog. Energy 42 (38), 23966–23985.
Hernández-Gómez, Á., Ramirez, V., Guilbert, D., Saldivar, B., 2021. Cell voltage static-dynamic modeling of a PEM electrolyzer based on adaptive parameters: Development and experimental validation. Renew. Energy 163, 1508–1522.
International Energy Agency, 2022. Global hydrogen review.
Koponen, J., Ruuskanen, V., Kosonen, A., Niemelä, M., Ahola, J., 2018. Effect of converter topology on the specific energy consumption of alkaline water electrolyzers. IEEE Trans. Power Electron. 34 (7), 6171–6182.
Krismer, F., Kolar, J.W., 2011. Efficiency-optimized high-current dual active bridge converter for automotive applications. IEEE Trans. Ind. Electron. 59 (7), 2745–2760.
LeRoy, R., Janjua, M., Renaud, R., Leuenberger, U., 1979. Analysis of time-variation effects in water electrolyzers. J. Electrochem. Soc. 126 (10), 1674.
Linde, 2024. Electrolysis for green hydrogen production towards a cleaner, greener future. https://www.linde.com/clean-energy/our-h2-technology/electrolysis-for-green-hydrogen-production. (Accessed: 04 April 2024).
Moutis, P., Alizadeh-Mousavi, O., 2020. Digital twin of distribution power transformer for real-time monitoring of medium voltage from low voltage measurements. IEEE Trans. Power Deliv. 36 (4), 1952–1963.
Oggier, G., Garcia, G.O., Oliva, A.R., 2010. Modulation strategy to operate the dual active bridge DC-DC converter under soft switching in the whole operating range. IEEE Trans. Power Electron. 26 (4), 1228–1236.
Pham, C.V., Escalera-López, D., Mayrhofer, K., Cherevko, S., Thiele, S., 2021. Essentials of high performance water electrolyzers–from catalyst layer materials to electrode engineering. Adv. Energy Mater. 11 (44), 2101998.
Rasheed, A., San, O., Kvamsdal, T., 2020. Digital twin: Values, challenges and enablers from a modeling perspective. IEEE Access 8, 21980–22012.
Rodríguez, J.R., Pontt, J., Silva, C., Wiechmann, E.P., Hammond, P.W., Santucci, F.W., Álvarez, R., Musalem, R., Kouro, S., Lezana, P., 2005. Large current rectifiers: State of the art and future trends. IEEE Trans. Ind. Electron. 52 (3), 738–746.
She, X., Huang, A.Q., Ni, X., 2013. Current sensorless power balance strategy for DC/DC converters in a cascaded multilevel converter based solid state transformer. IEEE Trans. Power Electron. 29 (1), 17–22.
Shi, J., Gou, W., Yuan, H., Zhao, T., Huang, A.Q., 2011. Research on voltage and power balance control for cascaded modular solid-state transformer. IEEE Trans. Power Electron. 26 (4), 1154–1166.
Shin, Y., Oh, J., Jang, D., Shin, D., 2022. Digital twin of alkaline water electrolysis systems for green hydrogen production. In: Computer Aided Chemical Engineering, vol. 49, Elsevier, pp. 1483–1488.
Siebert, A., Troedson, A., Ebner, S., 2002. AC to DC power conversion now and in the future. IEEE Trans. Ind. Appl. 38 (4), 934–940.
Solanki, J., Fröhleke, N., Böcker, J., 2015a. Implementation of hybrid filter for 12-pulse thyristor rectifier supplying high-current variable-voltage DC load. IEEE Trans. Ind. Electron. 62 (8), 4691–4701.
Solanki, J., Fröhleke, N., Böcker, J., Averberg, A., Wallmeier, P., 2015b. High-current variable-voltage rectifiers: state of the art topologies. IET Power Electron. 8 (6), 1068–1080.
Ulleberg, Ø., 2003. Modeling of advanced alkaline electrolyzers: a system simulation approach. Int. J. Hydrog. Energy 28 (1), 21–33.
Ursúa, A., Sanchis, P., 2012. Static–dynamic modelling of the electrical behaviour of a commercial advanced alkaline water electrolyser. Int. J. Hydrog. Energy 37 (24), 18598–18614.
Venkatesan, S., Manickavasagam, K., Tengenkai, N., Vijayalakshmi, N., 2019. Health monitoring and prognosis of electric vehicle motor using intelligent-digital twin. IET Electr. Power Appl. 13 (9), 1328–1335.
Wen, H., Xiao, W., Su, B., 2014. Nonactive power loss minimization in a bidirectional isolated DC–DC converter for distributed power systems. IEEE Trans. Ind. Electron. 61 (12), 6822–6831.
Zhang, K., Liang, X., Wang, L., Sun, K., Wang, Y., Xie, Z., Wu, Q., Bai, X., Hamdy, M.S., Chen, H., et al., 2022a. Status and perspectives of key materials for PEM electrolyzer. Nano Res. Energy 1 (3), e9120032.
Zhang, H., Lu, Y., Zhang, J., Benigni, A., 2022b. Real-time simulation of an electrolyzer with a diode rectifier and a three-phase interleaved buck converter. In: 2022 IEEE 13th International Symposium on Power Electronics for Distributed Generation Systems. PEDG, pp. 1–6. http://dx.doi.org/10.1109/PEDG54999.2022.9923192.
Zhao, B., Song, Q., Liu, W., 2013. Experimental comparison of isolated bidirectional DC–DC converters based on all-Si and all-SiC power devices for next-generation power conversion application. IEEE Trans. Ind. Electron. 61 (3), 1389–1393.
Zhao, B., Song, Q., Liu, W., Xiao, Y., 2012a. Next-generation multi-functional modular intelligent UPS system for smart grid. IEEE Trans. Ind. Electron. 60 (9), 3602–3618.
Zhao, T., Wang, G., Bhattacharya, S., Huang, A.Q., 2012b. Voltage and power balance control for a cascaded H-bridge converter-based solid-state transformer. IEEE Trans. Power Electron. 28 (4), 1523–1532.
Zhou, M., Yan, J., 2018. A new solution architecture for online power system analysis. CSEE J. Power Energy Syst. 4 (2), 250–256.